

# Microscopic Theory of Resistive Switching in Ordered Insulators: Electronic vs. Thermal Mechanism

Jiajun Li,<sup>†</sup> Camille Aron,<sup>‡,¶</sup> Gabriel Kotliar,<sup>§</sup> and Jong E. Han<sup>\*,†</sup>

<sup>†</sup>*Department of Physics, State University of New York at Buffalo, Buffalo, New York  
14260, USA*

<sup>‡</sup>*Laboratoire de Physique Théorique, École Normale Supérieure, CNRS, PSL Research  
University, Sorbonne Universités, 75005 Paris, France*

<sup>¶</sup>*Instituut voor Theoretische Fysica, KU Leuven, Belgium*

<sup>§</sup>*Department of Physics, Rutgers University, New Jersey 08854, USA*

E-mail: jonghan@buffalo.edu

## Abstract

We investigate the dramatic switch of resistance in ordered correlated insulators, when driven out of equilibrium by a strong voltage bias. Microscopic calculations on a driven-dissipative lattice of interacting electrons explain the main experimental features of resistive switching (RS), such as the hysteretic  $I$ - $V$  curves and the formation of hot conductive filaments. The energy-resolved electron distribution at the RS reveals the underlying nonequilibrium electronic mechanism, namely Landau-Zener tunneling, and also justifies a thermal description where the hot-electron temperature, estimated from the first moment of the distribution, matches the equilibrium phase transition temperature. We discuss the tangled relationship between filament growth and negative

differential resistance, and the influence of crystallographic structure and disorder in the RS.

Keywords: Resistive switching, Nonequilibrium phase transition, Landau-Zener tunneling, Joule heating, Nonequilibrium Green's function method

A variety of correlated oxides<sup>1-9</sup> experience a sudden change of resistivity by several orders of magnitude when subject to strong external electric fields of  $10^2 \sim 10^4$  V/cm. This nonequilibrium phase transition, referred as resistive switching (RS), shows hysteretic  $I$ - $V$  characteristics essential for new electronic memory/switching devices. The switching mechanisms in the RS have been debated for the last few decades without consensus, and a microscopic understanding of its underlying mechanism is now essential for continued progress in the field. Two underlying mechanisms to RS have been proposed: (1) electronic mechanism: direct effect of the electric field such as a dielectric breakdown due to electrons tunneling across the Mott gap,<sup>10-14</sup> and (2) thermal mechanism: indirect effect of the electric field with a thermally-induced phase transition due to Joule heating which locally melts the insulator.<sup>15-22,25</sup> The latter has recently received a strong experimental support in Ref.<sup>21</sup> where the local temperature could be monitored directly as the sample was bias-voltage-driven through the RS. Both these scenarios have been considered disconnected, and a question central to this intense debate is whether they are compatible or mutually exclusive.

The RS in vanadium oxides such as vanadium dioxide ( $\text{VO}_2$ ) and sesquioxide ( $\text{V}_2\text{O}_3$ ) have received much theoretical and experimental attention. In equilibrium, these prototypical Mott insulators exhibit a temperature-driven insulator-to-metal phase transition between an ordered insulator (with dimerized vanadium pairs in  $\text{VO}_2$  and antiferromagnetism in  $\text{V}_2\text{O}_3$ ) and a disordered metal with a resistivity drop of four orders of magnitude.<sup>23,24</sup> Out of equilibrium, the RS provoked by a strong voltage bias is accompanied with the formation of conductive filaments along the electric field.<sup>25,26</sup> These filaments were interpreted as electrical instabilities related to the peculiar S-shaped  $I$ - $V$  characteristics measured in  $\text{VO}_2$ , in particular to their region of negative differential resistance (NDR).<sup>27-30</sup>

Only a comprehensive microscopic theory of RS in correlated insulators, compatible with all the experimental evidence at hand, can resolve this long-standing puzzle. The recently proposed classical resistor network models<sup>1,2,20,31–34</sup> successfully reproduced part of the phenomenology but these are heuristic approaches, not firmly grounded from a microscopic perspective. In this work, we explain and reproduce the main features of RS listed above starting from a generic microscopic model which includes broken symmetry, drive and dissipative mechanisms, and the spatial inhomogeneity<sup>35,36</sup> for nonequilibrium phase-segregation. The quantum calculation further provides important information on the origin of the nonequilibrium excitations and on how the electronic and thermal RS scenarios are connected.

Our microscopic description consists of a slab of correlated electrons of length  $L$ , a Hubbard model, which is placed between two metallic leads.<sup>37–42</sup> A voltage bias  $V_s$  across the sample, and the resulting static electric field  $E = V_s/L$ , is created by connecting the two leads in series with a resistor  $R$  and a dc-voltage generator delivering a total voltage  $V_t = V_s + RI$ , with the current  $I$ . In addition to the dissipation by the two leads at the boundaries,<sup>13,41,43</sup> we also introduce energy relaxation in the bulk.<sup>37</sup> Both the external resistor and the energy dissipation are essential modeling ingredients that were overlooked in previous theoretical approaches of RS. The resistor is crucial to reveal a non-trivial regime of negative  $dI/dV_s$ , and dissipation is crucial to avoid overheating the sample.

We divide the Hamiltonian  $\hat{H}$  into (i)  $\hat{H}_{\text{Hub}}$ , the correlated electronic sample itself, given by a Hubbard model on a finite 2d square lattice, (ii)  $\hat{H}_{\text{bath+leads}}$ , the two leads and the dissipative environment, given by reservoirs of fermions, and (iii)  $\hat{H}_E$ , the electric-field induced electrostatic potential, originating from our choice to work with the Coulomb gauge.<sup>37,44</sup> We have

$$\hat{H}_{\text{Hub}} = -t \sum_{\langle \mathbf{r}\mathbf{r}' \rangle \sigma} (d_{\mathbf{r}\sigma}^\dagger d_{\mathbf{r}'\sigma} + \text{H.c.}) + \sum_{\mathbf{r}\sigma} \Delta \epsilon_{\mathbf{r}} d_{\mathbf{r}\sigma}^\dagger d_{\mathbf{r}\sigma} + U \sum_{\mathbf{r}} \Delta n_{\mathbf{r}\uparrow} \Delta n_{\mathbf{r}\downarrow}, \quad (1)$$

where  $d_{\mathbf{r}\sigma}^\dagger$  is the fermionic creation operator in the orbital at site  $\mathbf{r}$  with spin  $\sigma = \uparrow, \downarrow$ , and  $\Delta n_{\mathbf{r}\sigma} \equiv d_{\mathbf{r}\sigma}^\dagger d_{\mathbf{r}\sigma} - 1/2$ . The hopping integrals given by  $t$  are limited to nearest neighbors,

while  $U$  controls the on-site Coulombic interaction. To model grain boundaries and defects in realistic devices, we introduce the possibility of disorder with site-dependent energy levels  $\Delta\epsilon_{\mathbf{r}}$ . We set  $\hbar = e = a = 1$  where  $a$  is the lattice spacing and  $e$  the electron charge. Below, we work in units of  $t$ .

The dissipative environment consists of non-interacting fermion reservoirs coupled to every lattice site.<sup>10,44–46</sup> Two non-interacting leads are connected at the sample boundaries. Reservoirs and leads are in equilibrium at a temperature  $T_{\text{bath}}$  that we set to zero unless otherwise stated, we collect them in

$$\hat{H}_{\text{bath} + \text{leads}} = \sum_{\mathbf{r}\alpha\sigma} \epsilon_{\alpha} c_{\mathbf{r}\alpha\sigma}^{\dagger} c_{\mathbf{r}\alpha\sigma} - \sum_{\mathbf{r}\alpha\sigma} g_{\mathbf{r}} (d_{\mathbf{r}\sigma}^{\dagger} c_{\mathbf{r}\alpha\sigma} + \text{H.c.}). \quad (2)$$

The  $c_{\mathbf{r}\sigma\alpha}^{\dagger}$ 's represent the orbitals of the reservoirs at sites  $\mathbf{r}$  in the bulk or at the boundaries, and  $\alpha$  is the continuum index in each reservoir. The coupling to the reservoirs is given by  $g_{\mathbf{r}}$ . We simply consider infinite flat bands for the reservoirs dispersions  $\epsilon_{\alpha}$  and the coupling to the reservoirs yields a frequency-independent hybridization parameter  $\Gamma_{\mathbf{r}} = \pi |g_{\mathbf{r}}|^2 \sum_{\alpha} \delta(\omega - \epsilon_{\alpha})$ , which sets the rate at which particles/energy are exchanged with the environment. For the leads, we use  $\Gamma_{\mathbf{r}} = \Gamma_{\text{lead}} = 1.0$  while the bulk damping rate is set to  $\Gamma_{\mathbf{r}} = \Gamma = 0.01$ . The RS is essentially a bulk nonequilibrium phenomenon and, without the bulk dissipation, the effective temperature in the steady-state cannot be realistic<sup>47</sup> away from the leads.

Finally, with the voltage bias along the  $y$ -direction, the electrostatic potential is given by  $\varphi(\mathbf{r}) = -yE$  and

$$\hat{H}_E = \sum_{\mathbf{r}\sigma} \varphi(\mathbf{r}) \left( d_{\mathbf{r}\sigma}^{\dagger} d_{\mathbf{r}\sigma} + \sum_{\alpha} c_{\mathbf{r}\alpha\sigma}^{\dagger} c_{\mathbf{r}\alpha\sigma} \right). \quad (3)$$

To gain insight into the RS, we employ the Hartree-Fock (HF) approximation to treat the Coulombic interaction in  $\hat{H}_{\text{Hub}}$ . In equilibrium, this self-consistent mean-field approach produces a phase transition between a high-temperature low- $U$  paramagnetic metal (PM) and a low-temperature large- $U$  antiferromagnetic insulator (AFI). The corresponding order

parameter is the alternating local order  $\Delta_{\mathbf{r}}$  defined as  $U\langle n_{\mathbf{r}\sigma} \rangle = (-1)^{n_x+n_y} \Delta_{\mathbf{r}}$  with the lattice coordinates  $\mathbf{r} = (n_x, n_y)$ . The retarded and lesser Green's functions for the  $d$ -orbitals are computed in the steady state via Schwinger-Dyson's equations  $[\mathbf{G}_{\sigma}^{\text{R}}(\omega)]_{\mathbf{r}\mathbf{r}'}^{-1} = [\omega - \Delta\epsilon_{\mathbf{r}} - \varphi(\mathbf{r}) - U\langle \Delta n_{\mathbf{r},-\sigma} \rangle + i\Gamma_{\mathbf{r}}]\delta_{\mathbf{r}\mathbf{r}'} + t\delta_{\langle \mathbf{r}\mathbf{r}' \rangle}$  and  $G_{\sigma}^{<}(\omega)_{\mathbf{r}\mathbf{r}} = \sum_{\mathbf{s}} |G_{\sigma}^{\text{R}}(\omega)_{\mathbf{r}\mathbf{s}}|^2 \Sigma_{\mathbf{s}}^{<}(\omega)$ , respectively. The summation is over all lattice sites  $\mathbf{s}$  and the lesser electron self-energy originates from the reservoirs:  $\Sigma_{\mathbf{r}}^{<}(\omega) = 2i\Gamma_{\mathbf{r}}f_0(\omega - \mu_{\mathbf{r}})$  with the Fermi-Dirac (FD) distribution  $f_0(\epsilon) = [1 + \exp(\epsilon/T_{\text{bath}})]^{-1}$  and the local chemical potential  $\mu_{\mathbf{r}} = \varphi(\mathbf{r})$ . For any given voltage  $V_{\text{t}}$  delivered by the dc-generator, we solve the problem self-consistently without assuming a specific voltage profile in the sample.<sup>13,41</sup> Starting from an educated guess, we compute (i)  $G_{\sigma}^{\text{R}}(\omega)_{\mathbf{r}\mathbf{r}'}$ , (ii)  $G_{\sigma}^{<}(\omega)_{\mathbf{r}\mathbf{r}}$ , (iii)  $\langle \Delta n_{\mathbf{r},\sigma} \rangle$  and the total current  $I$ , (iv) the voltage bias  $V_{\text{s}} = V_{\text{t}} - RI$  ( $R$  is set to 1.2 throughout this work) and the electric field  $E$ , and we iterate until convergence is achieved. We then repeat the procedure by incrementally changing the total voltage to  $V_{\text{t}} + dV$  with a small  $dV$ , and complete the  $I$ - $V$  loop. To prevent the current leak into the fermion baths, we slightly adjust their chemical potential at each iteration.<sup>48</sup> While the model is constructed with an AF order, the discussion can be generalized to other ordered systems.

Let us first discuss the mechanism by which the interplay of drive and dissipation brings the system to a RS. Within a purely thermal scenario, one would argue that the nonequilibrium drive effectively enters this problem only as an effective temperature,  $T_{\text{eff}}(E)$ , caused by Joule heating. However, given the strongly discontinuous and hysteretic RS that are experimentally observed, the underlying mechanism must go beyond this simple reparametrization of the equilibrium theory. We address this puzzle by first considering an infinite and uniform system ( $L \rightarrow \infty$  keeping  $E$  fixed and  $\Delta\epsilon_{\mathbf{r}} = 0$ ), where the formalism developed in Ref.<sup>37</sup> can be readily applied to search for uniform steady-state solutions. In equilibrium ( $E = 0$ ), the Slater HF theory<sup>49</sup> predicts a continuous AFI/PM phase transition at the Néel temperature  $T_{\text{bath}} = T_{\text{N}}$ . FIG. 1(a) shows the mean-field conditions on the order parameter  $\Delta = F(\Delta; E, T_{\text{bath}}, \Gamma) = \frac{1}{2}U\langle n_{\uparrow} - n_{\downarrow} \rangle$ . At  $T_{\text{bath}} < T_{\text{N}}$ , there is only one stable AFI solution

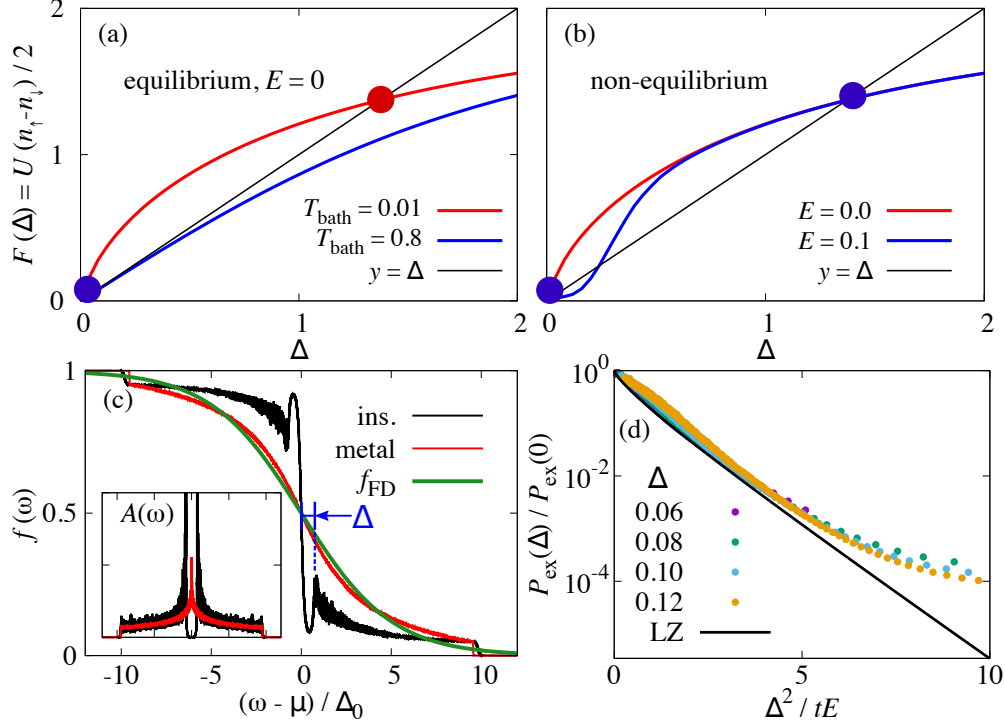


Figure 1: (a-b) Mean-field condition,  $\Delta = F(\Delta; E, T_{\text{bath}}, \Gamma) = \frac{1}{2}U\langle n_{\uparrow} - n_{\downarrow} \rangle$ , for an antiferromagnetic order parameter in an infinite uniform Hubbard model subject to dissipation. The stable solutions are marked with dots. (a) At  $E = 0$ , the antiferromagnetic insulator (AFI) goes continuously to the paramagnetic metal (PM)  $\Delta = 0$  upon increasing bath temperature  $T_{\text{bath}}$ . (b) At finite  $E$ , Joule heating in the metallic side increases the effective temperature  $T_{\text{eff}} > T_{\text{bath}}$ , stabilizing the PM solution and resulting in a bi-stable regime. (c) Local energy distribution function  $f(\omega)$  of insulating (black) and metallic (red) phases. The Fermi-Dirac function at an effective temperature is shown (green curve,  $T_{\text{eff}} = 1.05$ ) for comparison. Inset: corresponding density of states. (d) Total number of nonequilibrium excitations above the chemical potential,  $P_{\text{ex}}(\Delta)$ . Over a wide range of gaps,  $P_{\text{ex}}(\Delta)$  is well described by the Fermi-surface averaged Landau-Zener (LZ) tunneling rate<sup>48</sup> ( $\Gamma = 0.001$ ).

at a finite  $|\Delta| = \Delta_0$  which continuously goes to the PM solution  $\Delta = 0$  as  $T_{\text{bath}} > T_N$ . The nonequilibrium situation ( $E > 0$ ) in FIG. 1(b) is dramatically different. There are now two stable solutions<sup>50</sup> at low  $T_{\text{bath}}$ : an AFI solution at the equilibrium value  $\Delta \approx \Delta_0$  and the PM solution at  $\Delta = 0$  which was previously unstable. The latter can be explained within the thermal mechanism with a high effective temperature  $T_{\text{eff}} \propto E/\Gamma$  caused by Joule heating on the metallic side,<sup>37,44,46</sup> whereas on the insulating side the large gap prevents such an effect. The intermediate solution is unstable. The bi-stability of the order parameter results in heterogeneous phases during the RS, with an insulator-to-metal transition (IMT) with increasing electric field, and a metal-to-insulator transition (MIT) with decreasing electric field.

The mechanism underlying the RS is revealed by the local energy distribution function  $f_{\mathbf{r}}(\omega) = -\frac{1}{2}\text{Im}G_{\sigma}^{<}(\omega)_{\mathbf{r}\mathbf{r}}/\text{Im}G_{\sigma}^{\text{R}}(\omega)_{\mathbf{r}\mathbf{r}}$ , see FIG. 1(c). At finite  $E$ -fields, the metallic and insulating distributions deviate from the FD distribution. Note that, despite the similar overall shape, the metallic nonequilibrium distribution has a different functional expression<sup>46</sup> from the FD function (green curve). In the insulating phase, there are significant nonequilibrium excitations beyond the gap  $\Delta$ . The total number of nonequilibrium excitations above the bath chemical potential is plotted in FIG. 1(d) for a wide range of gaps. The agreement with the Landau-Zener (LZ) tunneling rate<sup>51</sup> shows that it is this electronic mechanism which is responsible for the RS: the electric field accelerates the quasi-particles in the lower band, which have a finite probability to tunnel across the gap  $\Delta$  and populate the higher band, rendering the system metallic. As described above,  $\Delta$  is the self-consistent result of the balance of the electronic interactions, the non-equilibrium drive and the dissipative mechanisms. As we shall see below and in Ref.,<sup>48</sup> this picture is still compatible with a thermal description where the nonequilibrium excitations are simply interpreted as thermal excitations. The deviation in the small  $E$  (or large  $\Delta^2/tE$ ) limit is due to the dephasing provided by the fermion baths.

Having demonstrated the basic mechanism of the RS, we now focus on the realistic

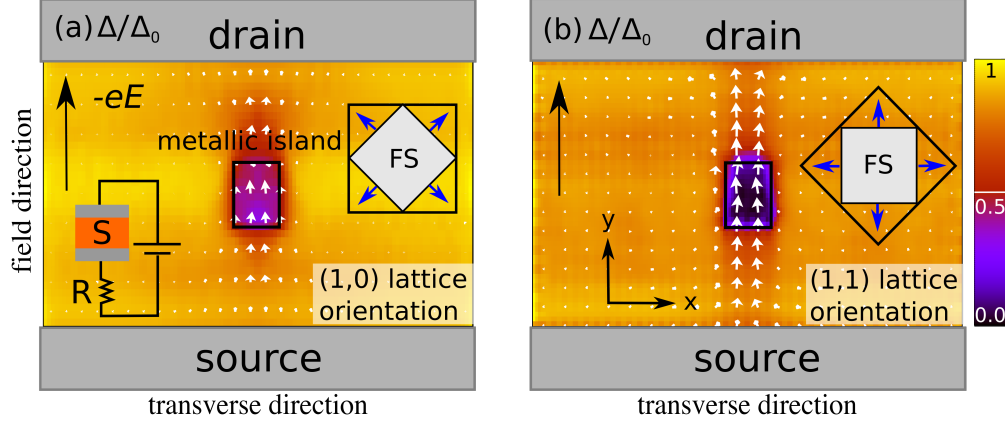


Figure 2: Nucleation of a conductive filament in an insulating sample driven by a voltage bias (see the left inset for a sketch of the setup) and in the presence of a metallic island. The color map gives the amplitude of the antiferromagnetic (AF) order parameter and the white arrows show the current distribution (direction and amplitude). (a) Sample cut along the (10)-direction: no filament, the current barely flows outside the impurity. (b) Sample cut along the (11)-diagonal: a robust conductive filament forms through the impurity, a strong current flows between the leads. Right insets: Fermi surfaces and Fermi-velocity vectors in blue.  $E/\Delta_0 = 0.252$  with the equilibrium gap  $\Delta_0 = 1.35$ ,  $U = 4.0$  and  $T_{\text{bath}} = 0.3$ .

phenomenology in finite and non-uniform samples. As we anticipate that the presence of weak disorder in the form of impurities or defects may favor the stabilization of mixed phases, we first investigate the role of spatial inhomogeneities by creating a  $5 \times 5$  metallic island (setting  $\Delta\epsilon_r = 1.5t$ ) at the center of an insulating sample with 1200 lattice sites with size  $(80a/\sqrt{2}) \times (30a/\sqrt{2})$ . In FIG. 2, we monitor the local order parameter  $\Delta_r$  and the local current for two different crystallographic orientations of the square lattice: (a) the sample is cut along the (10)-direction, and (b) along the (11)-diagonal. In the former case the RS occurs homogeneously, *i.e.* without noticeable pattern formation, at switching fields close to the values obtained with an infinite and homogeneous lattice. Yet, in the latter case we found strong and collimated filaments at much weaker fields.

This remarkable anisotropy can be traced to the Fermi surface geometry of the half-filled square lattice. In a (11)-lattice, the Fermi-velocity vector  $\mathbf{v}_F$  is aligned with the electric field, see the inset of FIG. 2 (b), making the diagonal direction an easy-axis for filament formation. This anisotropy is supported analytically in the non-interacting and weak-field limit,



where the nonequilibrium distribution function can be described by an anisotropic effective temperature  $T_{\text{eff}}(\mathbf{E}) \sim |\mathbf{v}_F \cdot \mathbf{E}|/\Gamma$ . See Ref.<sup>48</sup> for a detailed discussion. In polycrystalline samples, the filaments are expected to be globally aligned along  $\mathbf{E}$ , but with domain walls locally aligned along  $\mathbf{v}_F$ .

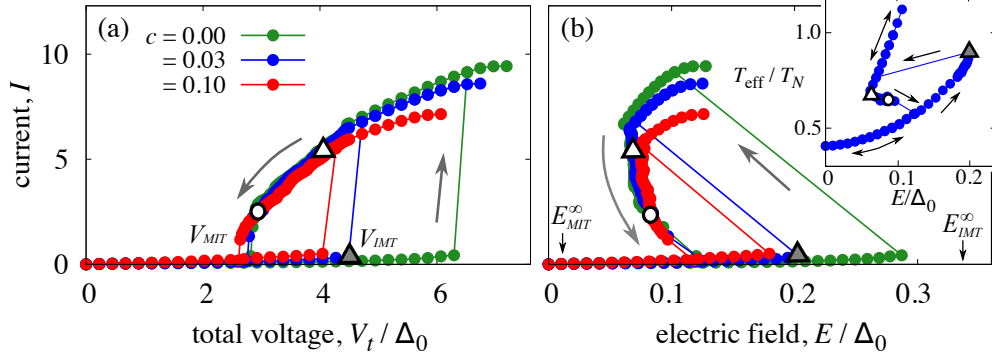


Figure 3:  $I$ - $V$  curves of a rectangular sample cut along the (11)-diagonal for different concentrations  $c$  given in the key.  $V_t$  is increased then decreased (marked by arrows). (a) Current as a function of the total voltage  $V_t$ . Contrary to the MIT, the IMT is strongly affected by the impurity concentration. (b) Current as a function of the electric field. When decreasing  $V_t$ , there is a region of negative  $dI/dV_s$ <sup>21,29</sup> caused by a narrowing metallic filament.  $E_{\text{MIT}}^{\infty}$  and  $E_{\text{IMT}}^{\infty}$  indicate the threshold fields of the infinite uniform lattice. In the inset of (b), the averaged effective temperature at  $c = 0.03$  displays an hysteretic behavior around the IMT at  $T_{\text{eff}} \approx T_N$ . The upward kink near the white triangle, down the metallic line, is a finite-size effect to disappear in the limit of a large system. Same parameters as in FIG. 2.

We now turn to a model where metallic impurities are randomly distributed at a fixed concentration  $c$ . FIG. 3 shows the hysteretic behavior of the current for different impurity concentrations as a function of (a) the total voltage  $V_t$ , and (b) the electric field  $E$ . The corresponding RS fields are found to be fractions of the equilibrium order parameter,  $E/\Delta_0 \sim 0.2$  (see also FIG. 4). Moreover, the IMT threshold field,  $E_{\text{IMT}}$ , appears to be strongly reduced in the presence of impurities, while the MIT at  $E_{\text{MIT}}$  is barely affected. This difference is due to the distinct nature of the two switching mechanisms, as we shall discuss later.

We now ask whether the nucleation of the filaments at the RS can be interpreted as the result of thermal excitations. We estimate the local effective temperature  $T_{\text{eff}}(\mathbf{r})$  as a first moment of the distribution function  $f_{\mathbf{r}}(\omega)$  via the Sommerfeld-like expansion  $\frac{\pi^2}{6} T_{\text{eff}}(\mathbf{r})^2 =$

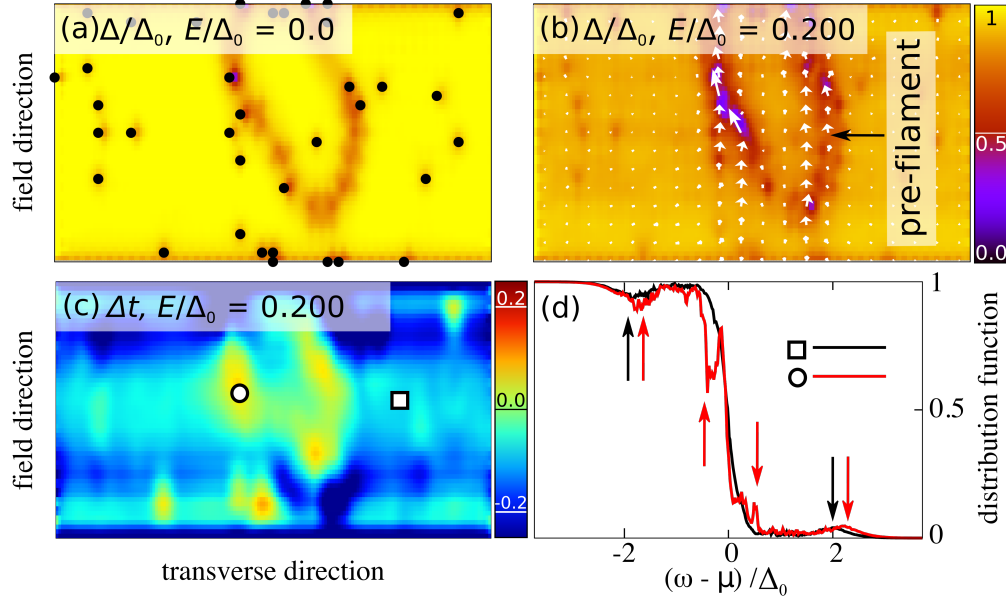


Figure 4: Pattern formation ahead of the IMT in a sample cut along the (11)-diagonal. (a)-(b) AF order parameter (color map) and current (white arrows) for increasing electric field. (a) At  $E = 0$ , the impurities (black dots) create a unique imprint on the AF order parameter. (b) At  $E/\Delta_0 = 0.200$  (grey triangle in Fig. 3), a conductive path (pre-filament) forms along the low- $\Delta$  region to trigger an IMT. (c) Effective temperature  $\Delta t \equiv (T_{\text{eff}} - T_N)/T_N$  distribution. Note the similarity with the current distribution in (b). (d) Nonequilibrium distribution function at sites marked in (c). The arrows point to strong nonequilibrium excitations. Same parameters as in FIG. 2 and  $c = 0.03$ .

$\int d\omega (\omega - \mu_{\mathbf{r}})[f_{\mathbf{r}}(\omega) - \theta(\mu_{\mathbf{r}} - \omega)]$ . Averaged over the whole sample,  $T_{\text{eff}}$  in the inset of Fig. 3(b) displays an hysteresis in excellent agreement with the one measured in  $\text{VO}_2$  in Ref.<sup>21</sup> In particular, at the IMT we find  $T_{\text{eff}} \approx T_{\text{N}} = 0.8$ , thus supporting the scenario of a thermally-driven IMT.

The nucleation of a filament at the IMT is a highly nonlinear process that we discuss in FIG. 4. (a) At  $E = 0$ , extended metallic inhomogeneities (darker zones) lie across the sample, and connect the two leads despite the concentration  $c = 0.03$  being far below the classical  $2d$  percolation threshold.<sup>52</sup> The precise pattern of these low- $\Delta$  paths is determined by the impurity distribution but, as a consequence of a quantum coherence length larger than the impurity spacing, it is not tightly bound to the impurity locations. These low- $\Delta$  paths will act as precursors for the filaments. At weak fields, they are not metallic enough to support any linear-response current. (b) Only very close to the IMT at  $E/\Delta_0 = 0.200$ , the filament is greatly reinforced and now supports a sizeable current. In (c), we plot the corresponding effective temperature distribution measured from the Néel temperature,  $\Delta t_{\mathbf{r}} \equiv [T_{\text{eff}}(\mathbf{r}) - T_{\text{N}}]/T_{\text{N}}$ . The temperature in the sample is approximately  $T_{\text{N}}$ , slightly hotter in the pre-filament region, and slightly cooler close to the leads that are maintained at  $T_{\text{bath}}$ . As shown in (d), the distribution function shows hotter region has stronger excitations.

Contrary to the IMT, the MIT is governed by the shrinking of the filaments upon reducing the bias. FIG. 5 (a) shows that the insulating domains start to nucleate from the edges of the sample parallel to the field at  $E/\Delta_0 = 0.068$ . This dependence of the MIT on the sample boundary geometry explains its rather weak dependence on the bulk impurities. As seen in FIG. 5 (b), the conducting filament shrinks as the  $E$ -field increases, leading to decreasing current. Remarkably, this filament dynamics results in the negative differential resistance (NDR)  $dI/dV_{\text{s}} < 0$  observed in FIG. 3 (b) and also reported in  $\text{VO}_2$ .<sup>21,25,26,29</sup> The NDR intrinsically originates from the nonequilibrium filament dynamics of the ordered solids and this branch of the  $I$ - $V$  is revealed by adding an external resistor. (See in Supporting Information<sup>48</sup> for more discussion.)

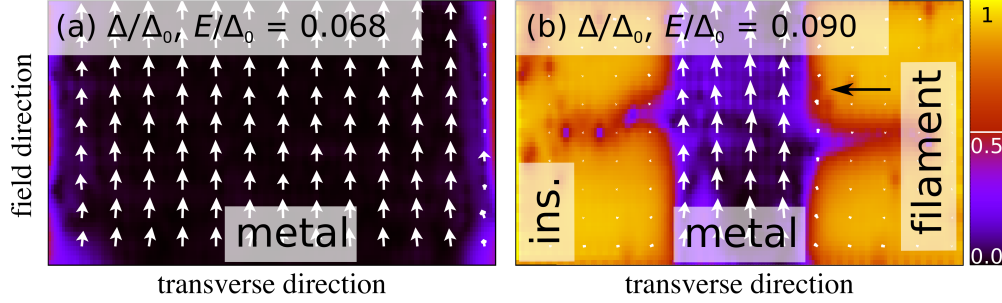


Figure 5: Filament formation ahead of the MIT. (a) At  $E/\Delta_0 = 0.068$  (white triangle in Fig. 3), the insulating solution nucleates on the sample edges parallel to the field. (b) When  $dI/dV_s < 0$  [see Fig. 3 (b)], the insulating domain grows from the edges, leaving a metallic filament which narrows progressively until the IMT at  $E/\Delta_0 = 0.090$  (white circle in Fig. 3).

To summarize, we have identified a minimal quantum driven-dissipative model that reproduces the main experimental signatures of RS in vanadium oxides. We showed that the RS is facilitated by a bi-stable insulator-metal phase which leads to the  $I$ - $V$  hysteresis, sudden nucleation of conducting filaments at the IMT, and the progressive narrowing of the filaments during the NDR regime ahead of the MIT. The RS is triggered by a Landau-Zener tunneling process across the self-consistently determined gap  $\Delta$ . We furthermore reconciled this electronic scenario with the Joule heating interpretation by showing how an effective temperature description could quantitatively reproduce the amount of excitations in the electronic system. Investigation by fempto-second STM or photoemission could resolve the dominant roles in the electronic and thermal mechanisms proposed in this work.

We are grateful to Petar Bakalov, Keshav Dani, Sambandamurthy Ganapathy, Pía Homm Jara, Hyun-Tak Kim, Mariela Menghini, Marcelo Rozenberg, Sujay Singh and for helpful discussions. We acknowledge the computational support at CCR (SUNY at Buffalo). This work has been supported by the NSF through the Grant No. DMR-1308141.

## References

- (1) Stoliar, P.; Cario, L.; Janod, E.; Corraze, B.; Guillot-Deudon, C.; Salmon-Bourmand, S.; Guiot, V.; Tranchant, J.; Rozenberg, M. *Adv. Mater.* **2013**, *25*, 3222.

- (2) Guiot, V.; Cario, L.; Janod, E.; Corraze, B.; Phuoc, V. Ta; Rozenberg, M.; Stoliar, P.; Cren, T.; Roditchev, D. *Nat. Commun.* **2013**, *4*, 1722.
- (3) Kumai, R.; Okimoto, Y.; Tokura, Y. *Science* **1999**, *284*, 1645.
- (4) Jeong, J.; Aetukuri, N.; Graf, T.; Schladt, T. D.; Samant, M. G.; Parkin, S. S. P. *Science* **2013**, *339*, 1402.
- (5) Inoue, I. H.; Yasuda, S.; Akinaga, H.; Takagi, H. *Phys. Rev. B* **2008**, *77*, 035105.
- (6) Lee, J. S.; Lee, S.; Noh, T. W. *Appl. Phys. Rev.* **2015**, *2*, 031303.
- (7) Lee, S.; Fursina, A.; Mayo, J. T.; Yavuz, C. T.; Colvin, V. L.; Sumesh Sofin, R. G.; Shvets, I. V.; Natelson, D. *Nat. Mat.* **2007**, *7*, 130.
- (8) Lee, S. B.; Chae, S. C.; Chang, S. H.; Lee, J. S.; Park, S.; Jo, Y.; Seo, S.; Kahng, B.; Noh, T. W. *Appl. Phys. Lett.* **2008**, *93*, 252102.
- (9) Shukla, N.; Joshi, T.; Dasgupta, S.; Borisov, P.; Lederman, D.; Datta, S. *Appl. Phys. Lett.* **2014**, *105*, 012108.
- (10) Tsuji, N.; Oka, T.; Aoki, H.; *Phys. Rev. B* **2008**, *78*, 235124.
- (11) Joura, A. V.; Freericks, J. K.; Pruschke, T. *Phys. Rev. Lett.* **2008**, *101*, 196401.
- (12) Oka, T.; Arita, R.; Aoki, H. *Phys. Rev. Lett.* **2003**, *91*, 066406.
- (13) Mazza, G.; Amaricci, A.; Capone, M.; Fabrizio, M. *Phys. Rev. B* **2015**, *91*, 195124.
- (14) Mazza, G.; Amaricci, A.; Capone, M.; Fabrizio, M. *Phys. Rev. Lett.* **2016**, *117*, 176401.
- (15) Chudnovskii, F. A.; Pergament, A. L.; Stefanovich, G. B.; Metcalf, P. A.; Honig, J. M. *J. Appl. Phys.* **1998**, *84*, 2643.
- (16) Brockman, J. S.; Gao, L.; Hughes, B.; Rettner, C. T.; Samant, M. G.; Roche, K. P.; Parkin, S. S. P. *Nat. Nanotechnol.* **2014**, *9*, 453.

- (17) Gu  non, S.; Scharinger, S.; Wang, S.; Ramirez, J. G.; Koelle, D.; Kleiner, R.; Schuller, I. K. *EPL Europhys. Lett.* **2013**, *101*, 57003.
- (18) Bae, S.-H.; Lee, S.; Koo, H.; Lin, L.; Jo, B. H.; Park, C.; Wang, Z. L. *Adv. Mater.* **2013**, *25*, 5098.
- (19) Nakamura, F.; Sakaki, M.; Yamanaka, Y.; Tamaru, S.; Suzuki, T.; Maeno, Y. *Sci. Rep.* **2013**, *3*, 2536.
- (20) Driscoll, T.; Kim, H.-T.; Chae, B.-G.; Di Ventra, M.; Basov, D. N. *Appl. Phys. Lett.* **2009**, *95*, 043503.
- (21) Zimmers, A.; Aigouy, L.; Mortier, M.; Sharoni, A.; Wang, S.; West, K. G.; Ramirez, J. G.; Schuller, I. K. *Phys. Rev. Lett.* **2013**, *110*, 056601.
- (22) Singh, S.; Horrocks, G.; Marley, P. M.; Shi, Z.; Banerjee, S.; Sambandamurthy, G. *Phys. Rev. B* **2015**, *92*, 155121.
- (23) Morin, F.; *Phys. Rev. Lett.* **1959**, *3*, 34.
- (24) Takei, H.; Koide, S. *J. Phys. Soc. Jpn.* **1966**, *21*, 1010.
- (25) Duchene, J.; Terraillon, M.; Pailly, P.; Adam, G. *Appl. Phys. Lett.* **1971**, *19*, 115.
- (26) Berglund, C. N. *IEEE Trans. Elec. Dev.* **1969**, *16*, 432.
- (27) Ridley, B. K. *Proc. Phys. Soc.* **1963**, *82*, 954.
- (28) Cope R. G.; Penn, A. W.; *Brit. J. Appl. Phys. (J. Phys. D)* **1968**, *1*, 161.
- (29) Kim, H.-T.; Kim, B.-J.; Choi, S.; Chae, B.-G.; Lee, Y. W.; Driscoll, T.; Qazilbash, M. M.; Basov, D. N. *J. Appl. Phys.* **2010**, *107*, 023702.
- (30) Kim, J.; Ko, C.; Frenzel, Alex.; Ramanathan, S.; Hoffman, J. E. *Appl. Phys. Lett.* **2010**, *96*, 213106.

- (31) Janod, E.; Tranchant, J.; Corraze, B.; Querré, M.; Stoliar, P.; Rozenberg, M.; Cren, T.; Roditchev, D.; Ta Phuoc, V.; Besland, M.-P.; Cario, L. *Adv. Funct. Mater.* **2015**, *25*, 6287.
- (32) Driscoll, T.; Quinn, J.; Di Ventura, M.; Basov, D. N.; Seo, G.; Lee, Y. W.; Kim, H.-T.; Smith, D. R. *Phys. Rev. B* **2012**, *86*, 094203.
- (33) Stoliar, P.; Rozenberg, M.; Janod, E.; Corraze, B.; Tranchant, J.; Cario, L. *Phys. Rev. B* **2014**, *90*, 045146.
- (34) Dubson, M. A.; Hui, Y. C.; Weissman, M. B.; Garland, J. C. *Phys. Rev. B* **1989**, *39*, 6807.
- (35) Potthoff, M.; Nolting, W. *Phys. Rev. B* **1999**, *60*, 7834.
- (36) Dobrosavljević, V.; Kotliar, G. *Phys. Rev. Lett* **1997**, *78*, 3943.
- (37) Li, J.; Aron, C.; Kotliar, G.; Han, J. E. *Phys. Rev. Lett.* **2015**, *114*, 226403.
- (38) Aron, C. *Phys. Rev. B* **2012**, *86*, 085127.
- (39) Amaricci, A.; Weber, C.; Capone, M.; Kotliar, G. *Phys. Rev. B* **2012**, *86*, 085110.
- (40) Neumayer, J.; Arrigoni, E.; Aichhorn, M.; von der Linden, W. *Phys. Rev. B* **2015**, *92*, 125149.
- (41) Okamoto, S. *Phys. Rev. Lett.* **2008**, *101*, 116807.
- (42) Aron, C.; Kotliar, G.; Weber, C. *Phys. Rev. Lett.* **2012**, *108*, 086401.
- (43) Ribeiro, P.; Antipov, A. E.; Rubtsov, A. N. *Phys. Rev. B* **2016**, *93*, 144305.
- (44) Han, J. E.; Li, J. *Phys. Rev. B* **2013**, *88*, 075113.
- (45) Han, J. E. *Phys. Rev. B* **2013**, *87*, 085119.

- (46) Mitra A.; Millis, A. J. *Phys. Rev. B* **2008**, *77*, 220404(R).
- (47) Without the bulk dissipation, the effective temperature inside the sample away from the leads reaches the energy scale  $\sim EL = V_s$ , unrealistically high value. Furthermore, the RS is controlled by  $E$ , not by  $EL$ .
- (48) See the Supporting Information.
- (49) Slater, J. C. *Phys. Rev.* **1951**, *82*, 538.
- (50) Sugimoto, N.; Onoda, S.; Nagaosa, N. *Phys. Rev. B* **2008**, *78*, 155104.
- (51) Zener, C. *Proc. R. Soc. Lond. A* **1932**, *137*, 696.
- (52) Reynolds, P. J. ; Stanley, H. E.; Klein, W. *Phys. Rev. B* **1980**, *21*, 1223.



Supporting Information:

# Microscopic Theory of Resistive Switching in Ordered Insulators: Electronic vs. Thermal Mechanism

Jiajun Li<sup>1</sup>, Camille Aron<sup>2,3</sup>, Gabriel Kotliar<sup>4</sup> and Jong E. Han<sup>1,\*</sup>

<sup>1</sup> *Department of Physics, State University of New York at Buffalo, Buffalo  
New York 14260, USA*

<sup>2</sup> *Laboratoire de Physique Théorique, École Normale Supérieure, CNRS  
PSL Research University, Sorbonne Universités, 75005 Paris, France*

<sup>3</sup> *Instituut voor Theoretische Fysica, KU Leuven, Belgium*

<sup>4</sup> *Department of Physics, Rutgers University, New Jersey 08854, USA*

\*corresponding author e-mail: [jonghan@buffalo.edu](mailto:jonghan@buffalo.edu)

## I. CURRENT AND CURRENT LEAK TO THE FERMION RESERVOIRS

The steady-state electric current between nearest neighbor sites  $\mathbf{r}$  and  $\mathbf{r} + \hat{\mathbf{e}}$  is evaluated as

$$I_{\mathbf{r},\hat{\mathbf{e}}} = -it \sum_{\sigma} (\langle d_{\mathbf{r}+\hat{\mathbf{e}}\sigma}^{\dagger} d_{\mathbf{r}\sigma} \rangle - \text{H.c.}) = -t \sum_{\sigma} \int \left[ G_{\mathbf{r}+\hat{\mathbf{e}},\mathbf{r}}^{<}(\omega) - G_{\mathbf{r},\mathbf{r}+\hat{\mathbf{e}}}^{<}(\omega) \right] \frac{d\omega}{2\pi}. \quad (1)$$

where the lesser Green's functions  $G_{\mathbf{r}\mathbf{r}'}^{<}(\omega)$  are expressed in Eq. (7).

While the role the two leads is to supply both particle and heat transfer to/from the sample, the purpose of the local fermion reservoirs is to provide energy relaxation only. A uniform steady-state current in an infinite homogeneous lattice does not yield any particle flux to the fermion reservoirs that constitute the thermostats when their chemical potential is set to  $\mu_{\mathbf{r}} = \varphi(\mathbf{r})$  [3]. However, in a finite or disordered lattice with a non-uniform current there can be a small volumic leakage of particles to the reservoirs, which can be expressed as

$$I_{\text{leak},\sigma\mathbf{r}} = -i \sum_{\alpha\sigma} g_{\mathbf{r}} (\langle d_{\mathbf{r}\sigma}^{\dagger} c_{\mathbf{r}\alpha\sigma} \rangle - \text{H.c.}) = 2\Gamma_{\mathbf{r}} \int d\omega A_{\sigma\mathbf{r}}(\omega) [f_{\sigma\mathbf{r}}(\omega) - f_0(\omega - \mu_{\mathbf{r}})], \quad (2)$$

with the local density of states  $A_{\sigma\mathbf{r}}(\omega) = -\pi^{-1} \text{Im } G_{\sigma}^{\text{R}}(\omega)_{\mathbf{r}\mathbf{r}}$  and the local nonequilibrium distribution function  $f_{\sigma\mathbf{r}}(\omega) = G_{\sigma}^{<}(\omega)_{\mathbf{r}\mathbf{r}} / (2\pi i A_{\sigma\mathbf{r}}(\omega))$ . Therefore, we slightly adjust the local chemical potential  $\mu_{\mathbf{r}}$  at each HF iteration to ensure the vanishing of  $I_{\text{leak},\sigma\mathbf{r}}$  and prevent any particle leak.

## II. NEGATIVE DIFFERENTIAL RESISTANCE SOLUTION VIA EXTERNAL RESISTOR

In this Section, we explain the relations between  $I(V_t)$  in FIG. 3(a) and  $I(V_s)$  in FIG. 3(b) of the Letter, and how to access the negative differential resistance (NDR) regime of the latter.

In FIG. 3(a), the current is plotted as a function of the total voltage imposed by the dc generator on the circuit,  $V_t$ .  $I(V_t)$  corresponds to what is directly measured in experiments. However, in order to characterize a sample independently of the details of the external electrical circuit, one is interested in giving the current versus the voltage drop across the sample,  $V_s$ .  $I(V_s)$  is the *intrinsic* characteristic of the sample, plotted in FIG. 3(b).

While both  $I(V_s)$  and  $I(V_t)$  are of course trivially related to one-another by Kirchhoff's laws, which in our case simply yield

$$V_t = V_s + RI, \quad (3)$$

the measurement of  $I(V_t)$  for all  $V_t$  does not guaranty the full knowledge of  $I(V_s)$ . Indeed, if the latter is non-monotonous or multivalued, parts of the  $I(V_s)$  characteristic will be inaccessible, *i.e.* hidden, unless the external resistance is selected with care [5].

To illustrate this point, let us re-write Eq. (3) as

$$\frac{V_t - V_s}{R} = I(V_s). \quad (4)$$

This expresses that fact that for a given  $V_t$  delivered by the dc generator, both  $I$  and  $V_s$  are self-consistent solutions that live at the intersection(s) of the line  $(V_t - V_s)/R$  (LHS) with the characteristic  $I(V_s)$  (RHS).

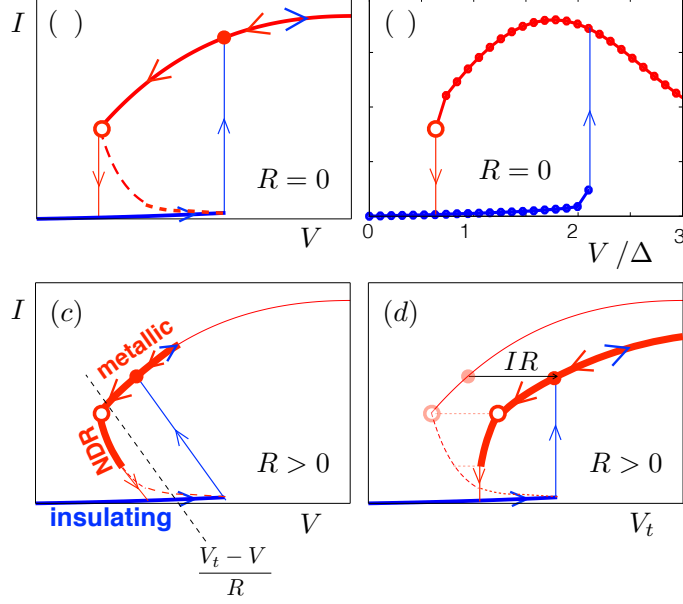


Figure S1: (a) Schematic  $I$ - $V$  plot with zero external resistance  $R = 0$  and (b) the actual numerical results ( $c = 0.03$ ). Schematic graphs (c) plotted against the sample voltage  $V_s$  with  $R > 0$  and (d) plotted against the total voltage  $V_t$  with  $R > 0$ . The blue (resp. red) arrows denote the solutions obtained when increasing (resp. decreasing) the total voltage  $V_t$ . White circles mark the first appearance of insulating regions on the edges of the metallic sample when decreasing  $V_t$  on the metallic branch.

In our case, we are dealing with S-shaped  $I(V_s)$  characteristics, for which the current happens to be multivalued for given values of the voltage, see the sketch in FIG. S1(a). Another case, which we shall not examine here, are N-shaped  $I(V_s)$  characteristics for which it is the voltage that is multivalued for a given current. In our case, the physical reason behind that peculiar S shape is the appearance (see the white circles in FIG. S1) and the rapid growth of insulating domains when reducing the voltage bias ahead of the MIT, as shown in FIG. 5(a-b) of manuscript. This causes an NDR regime,  $dI/dV_s < 0$ , which extends until the sample is fully metallic. For the discussion, we decompose the  $I(V_s)$  characteristic in three branches: the insulating branch, the metallic branch, and the NDR branch in the middle, see FIG. S1(a).

To understand why the NDR branch of the  $I(V_s)$  characteristic needs extra care to be revealed, let us first consider the case  $R = 0$  illustrated schematically in FIG. S1(a) and computed numerically in FIG. S1(b). At  $V_t = 0$ , there is a single trivial solution:  $I = 0$  and  $V_s = 0$ . As  $V_t$  is slowly increased, the solution remains by continuity on the insulating branch of the  $I(V_s)$  characteristic, even when two extra solutions have appeared on the other branches of the S. For larger voltages, when  $V_t = V_{\text{MIT}}$ , the insulating branch stops, and the current makes a brutal and discontinuous transition towards the solution on the metallic branch. As  $V_t$  is now slowly decreased, the system remains on the metallic branch, until it stops at  $V_t = V_{\text{MIT}}$ , where the current jumps back on the insulating branch. We see that without external resistance,  $R = 0$ , the system experiences a strong hysteresis making it impossible to probe the NDR branch of the  $I(V_s)$  characteristic, no matter the value of  $V_t$ .

It is not hard to show that the condition on the resistance to avoid any hysteresis loop, and

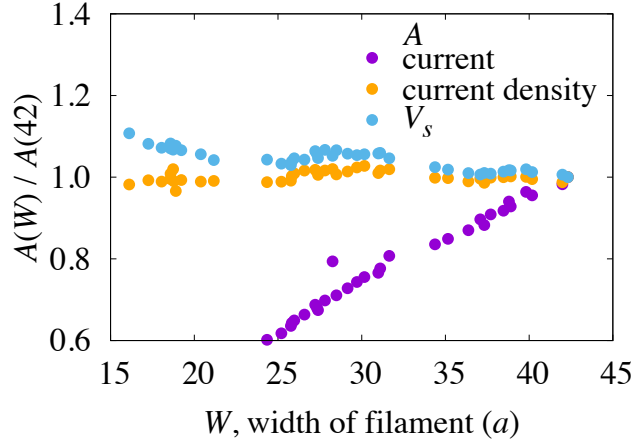


Figure S2: Current and sample voltage  $V_s$  as a function of the filament width  $W$  on the negative-differential-conductance branch. Inside the filament, the electric current density (measured and averaged along the central line of the filament) is nearly independent of  $W$  while the voltage slightly increases as the width decreases.

therefore probe the full NDR branch, is

$$R > R_{\min} \text{ with } \frac{1}{R_{\min}} \equiv \min \left\{ \left| \frac{dI(V_s)}{dV_s} \right| ; V_s \in [V_{\text{MIT}}, V_{\text{IMT}}] \right\}, \quad (5)$$

which guaranties a unique solution to Eq. (4) for all values of  $V_t$ . This is particularly clear in the limit  $R \rightarrow \infty$ , where the LHS of Eq. (4) is an horizontal line, always intersecting  $I(V_s)$  at a single point. Such a current-controlled measurement has been performed experimentally in Ref. [6], where the NDR branch was thereby fully uncovered.

In the intermediate cases,  $0 < R < R_{\min}$ , the NDR branch can only be partially revealed, as shown in FIG. S1(c). This is the case for the numerical data presented in the manuscript (the external resistance was set to  $R = 0.634$ ).

### III. NEGATIVE DIFFERENTIAL RESISTANCE MECHANISM

The NDR in the resistive switching is characterized by the metal-insulator coexistent phase. The main experimental observation is that the  $I$ - $V$  curve is very steep [6, 7] with the slope  $|dI/dV_s|$  decreasing with increasing sample bias  $V_s$ , which was reproduced by the calculation in the main text. The mechanism for the NDR can be understood as follows. As shown in Figure S2, the current density inside the filament is the property of the bulk metallic state and remains nearly constant as a function of the filament width  $W$ . Therefore, the total current is linearly proportional to  $W$ , as clearly shown in the figure. On the other hand, the voltage drop in the sample is given by the *resistivity* of the metallic state and current density, with the *resistance* being nearly independent of the current, leading to a vertical  $I$ - $V$  relation. However, as indicated by the data in the figure, the voltage drop slightly increases at small  $W$ , due to the enhanced scattering from domain boundaries of the filament. This opposite behavior of  $I$  and  $V$  as a function of the filament width is the origin of the NDR. For instance, an increase of current is mainly due to the growing filament width, which results in less electron scattering and reduced resistance and voltage drop across the sample.

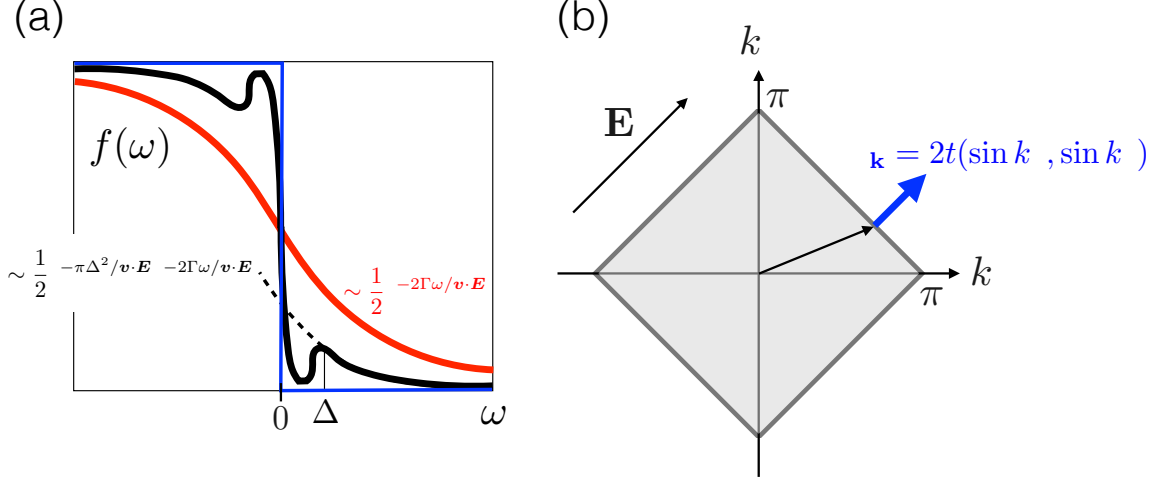


Figure S3: (a) Schematic plot of the local energy distribution function given in FIG. 1 of the Letter. The metallic distribution (red), with a tail  $\sim \frac{1}{2}e^{-\Gamma\omega/v\cdot E}$ , is reduced in the gapped phase (black) by the Landau-Zener factor  $e^{-\pi\Delta^2/v\cdot E}$  as outlined by the dashed line that fits most of the nonequilibrium energy distribution. The equilibrium distribution (blue) at  $E = 0$  is a step function because the environment is kept at zero temperature. (b) Fermi sea of a  $2d$  square lattice at half-filling. The electric field  $\mathbf{E}$  is oriented along the  $(1, 1)$  direction, as in FIG. 1 of the Letter.

This demonstrates that the NDR in the RS is an *intrinsic* property of the sample, independent of the external resistor. The external resistor only helps the algorithm to find the NDR branch out of the three possible stable solutions for  $E$ -field with  $E_{\text{MIT}} < E < E_{\text{IMT}}$ . We can numerically prove that the NDR is an intrinsic property of the sample, as follows. We proceed as in Figure S1(c) from the metallic branch by decreasing the total voltage  $V_t$ , and stop the simulation as soon as the NDR solution is found, right past the white circle. We then remove the external resistor from the circuit and increase the voltage which is now the sample voltage  $V_s$ . This procedure reproduces the same NDR  $I$ - $V$  relation as shown in Figure S1(c). This behavior was confirmed on the curves reported on the main text.

#### IV. ENERGY DISTRIBUTION FUNCTION

In this Section, we discuss the local energy distribution function which provides valuable quantum mechanical information about the nonequilibrium dynamics. It is defined as

$$f_{\mathbf{r}}(\omega) = -\frac{1}{2} \frac{\text{Im}G_{\sigma}^<(\omega)_{\mathbf{r}\mathbf{r}}}{\text{Im}G_{\sigma}^{\text{R}}(\omega)_{\mathbf{r}\mathbf{r}}}. \quad (6)$$

and reduces to the Fermi-Dirac function in equilibrium ( $E = 0$ ). Within the HF approximation, the lesser Green's function can be expressed as [3]

$$G_{\mathbf{r}\mathbf{r}'}^<(\omega) = 2i\Gamma \sum_{\mathbf{r}''} G_{\mathbf{r}\mathbf{r}''}^{\text{R}}(\omega) [G_{\mathbf{r}''\mathbf{r}'}^{\text{R}}(\omega)]^* f_0(\omega + \mathbf{r}'' \cdot \mathbf{E}), \quad (7)$$

and locally, we have

$$G_{\mathbf{0}\mathbf{0}}^<(\omega) = 2i\Gamma \sum_{\mathbf{r}} |G_{\mathbf{0}\mathbf{r}}^{\text{R}}(\omega)|^2 f_0(\omega + \mathbf{r} \cdot \mathbf{E}), \quad (8)$$

where  $f_0(\omega)$  is the Fermi-Dirac distribution of the fermion reservoirs maintained in equilibrium at temperature  $T_{\text{bath}}$ . In the case of a pure metal (non-interacting limit), it was already shown in Ref. [3] that the precise shape of the nonequilibrium distribution function is the result of superimposing the Fermi-Dirac distributions originating from the fermion reservoirs at distant sites with chemical potential governed by the bias potential  $\varphi(\mathbf{r})$ . It is the overall profile of the resulting nonequilibrium distribution that can be used to define an effective temperature  $T_{\text{eff}}$ , *a priori* much different from  $T_{\text{bath}}$ . See, for example, FIG. S2(a) where the driven metallic phase (in red) displays a hot  $T_{\text{eff}}$ . We shall discuss this effective temperature in more details in Sect. V. Noteworthy, one can interpret the above factor  $|G_{\mathbf{0}\mathbf{r}}^R(\omega)|^2$ , which is the wavefunction overlap between sites  $\mathbf{r}$  and  $\mathbf{0}$  due to quantum tunneling, as the coupling strength of the statistical information across the lattice. We emphasize that this nonequilibrium distribution is the result of electronic processes only. Therefore, it should establish itself much faster than a simple thermal diffusion process.

The above formal discussion on the electronic origin of the nonequilibrium distribution function can be corroborated by showing explicitly that the nonequilibrium excitations correspond to Landau-Zener tunneling processes (LZT) [9] over the gap  $\Delta$ . If this claim is correct, it implies that the nonequilibrium distribution functions of the metallic phase (where  $\Delta = 0$ ) and the insulating phase (where  $\Delta > 0$ ) mostly differ by a LZT factor  $e^{-\pi\Delta^2/|\mathbf{v}\cdot\mathbf{E}|}$ , as depicted schematically in FIG. S2(a). To test this claim, we compare the numerical results with the LZT predictions on the total number of nonequilibrium excitations above the chemical potential,

$$P_{\text{ex}}(\Delta) = \int_0^\infty A(\omega; \Delta) f(\omega; \Delta) d\omega, \quad (9)$$

where  $A(\omega) = -\pi^{-1}\text{Im}G_{\text{loc}}^R(\omega)$  is the local density of states. On the one hand, we compute Eq. (9) numerically. On the other hand, we estimate  $P_{\text{ex}}(\Delta)$  as the steady-state number of excitations in the presence of two competing processes: LZT events occurring at a rate  $\gamma_{\text{LZ}}(\Delta) \sim E \exp(-\pi\Delta^2/|\mathbf{v}\mathbf{k} \cdot \mathbf{E}|)$  (the precise numerical prefactor arises from the Bloch oscillations frequency), and relaxation events occurring at a rate  $\sim \Gamma$ . We therefore obtain, summed over the Fermi surface (FS),

$$P_{\text{ex}}(\Delta) = \frac{1}{\mathcal{S}_{\text{FS}}} \int_{\mathbf{k} \in \text{FS}} d\mathbf{k} \frac{\gamma_{\text{LZ}}(\Delta)}{\gamma_{\text{LZ}}(\Delta) + \Gamma}, \quad (10)$$

where  $\mathcal{S}_{\text{FS}}$  is the Fermi surface area. In our case of a  $2d$  square lattice with the field  $\mathbf{E}$  along the  $(1,1)$  diagonal, the group velocity at the half-filled Fermi surface is either parallel or perpendicular to  $\mathbf{E}$ . We can therefore reduce the Fermi surface integral to its first quadrant defined as  $k_x + k_y = \pi$  [see Fig. S2(b)], yielding the prediction

$$P_{\text{ex}}(\Delta) = \frac{1}{\pi} \int_0^\pi dk_x \frac{\frac{E}{\sqrt{2}} \exp\left(-\frac{\pi\Delta^2}{2\sqrt{2}tE \sin k_x}\right)}{\frac{E}{\sqrt{2}} \exp\left(-\frac{\pi\Delta^2}{2\sqrt{2}tE \sin k_x}\right) + \Gamma}. \quad (11)$$

In FIG. 1(d) of the Letter, we compare this LZT prediction with the numerics. They display an excellent agreement over several orders of magnitude of the gap  $\Delta$ . This demonstrates that the Landau-Zener tunneling is responsible for the nonequilibrium excitations.

## V. EFFECTIVE TEMPERATURE

In this Section, we discuss and justify the expression for the effective temperature

$$T_{\text{eff}} \sim \frac{|\mathbf{E} \cdot \mathbf{v}_F|}{\Gamma}, \quad (12)$$

which we use inside metallic domains to argue for the strong dependence of Joule heating on the crystallographic direction with respect to the field direction. Aside from this geometric consideration, note that this expression also transparently elucidated how Joule heating sets the temperature as the result of a balance between the drive  $\mathbf{E}$  and the energy relaxation rate  $\Gamma$ .

In the metallic regime, we can start by neglecting the on-site Coulomb interaction. Within a first-order gradient approximation, *i.e.* when the spatial and temporal inhomogeneities of the system occur on mesoscopic scales, the Quantum Boltzmann Equation governing the distribution function  $f_\sigma$  reads, dropping the spin index,

$$[\partial_T + \mathbf{v}(\mathbf{k}) \cdot \nabla_{\mathbf{X}} + \mathbf{E} \cdot \nabla_{\mathbf{k}}] f(X; k) = 2\Gamma [f_0(\omega - \mu_{\mathbf{X}}) - f(X; k)]. \quad (13)$$

Here,  $X = (T, \mathbf{X})$  are space-time coordinates and  $k = (\omega, \mathbf{k})$  are Fourier components. The velocity is given by  $\mathbf{v}(\mathbf{k}) = \nabla_{\mathbf{k}} \epsilon(\mathbf{k})$  where  $\epsilon(\mathbf{k})$  is the dispersion relation (square lattice in our case). Having neglected the Coulomb interactions, the collision integral on the RHS is only due to the scattering with the degrees of freedom of the local thermostats in equilibrium at temperature  $T_{\text{bath}}$  and chemical potential  $\mu_{\mathbf{X}} = -\mathbf{E} \cdot \mathbf{X}$ .  $f_0(\epsilon) \equiv [1 + \exp(\epsilon/T_{\text{bath}})]^{-1}$  is the Fermi-Dirac distribution. Once a steady state is reached, it simplifies to

$$[\mathbf{v}(\mathbf{k}) \cdot \nabla_{\mathbf{X}} + \mathbf{E} \cdot \nabla_{\mathbf{k}}] f(X; k) = 2\Gamma [f_0(\omega + \mathbf{E} \cdot \mathbf{X}) - f(X; k)]. \quad (14)$$

If analyzing this equation order by order in  $\mathbf{E}$ , *i.e.* decomposing  $f(\mathbf{X}; k) = f_0(\omega) + \mathbf{E} \cdot \mathbf{f}^{(1)} + E_i E_j f_{ij}^{(2)} + \dots$ , one can check that the contribution from the term in  $\mathbf{E} \cdot \nabla_{\mathbf{k}}$  in Eq. (14) is of higher order than those of the other terms and can therefore be neglected in a first approximation. Therefore we simplify further the equation to work with

$$\mathbf{v}(\mathbf{k}) \cdot \nabla_{\mathbf{X}} f(X; k) = 2\Gamma [f_0(\omega + \mathbf{E} \cdot \mathbf{X}) - f(X; k)]. \quad (15)$$

In the limit of zero-temperature thermostats,  $T_{\text{bath}} \rightarrow 0$ , we obtain the following solution

$$f(\mathbf{X}; \omega, \mathbf{k}) = \Theta(-\omega - \mathbf{E} \cdot \mathbf{X}) + \frac{1}{2} [\text{sign}(\omega + \mathbf{E} \cdot \mathbf{X}) + \text{sign}(\mathbf{E} \cdot \mathbf{v}(\mathbf{k}))] \exp\left(-2\Gamma \left| \frac{\omega + \mathbf{E} \cdot \mathbf{X}}{\mathbf{E} \cdot \mathbf{v}(\mathbf{k})} \right| \right). \quad (16)$$

where  $\Theta(\epsilon)$  is the Heaviside step function. For wave-vectors  $\mathbf{k}^*$  such that  $\mathbf{E} \perp \mathbf{v}(\mathbf{k}^*)$ , this simplifies to

$$f(\mathbf{X}; \omega, \mathbf{k}^*) = \Theta(-\omega - \mathbf{E} \cdot \mathbf{X}), \quad (17)$$

which is the zero-temperature Fermi-Dirac distribution,  $\lim_{T_{\text{bath}} \rightarrow 0} f_0(\omega - \mu_{\mathbf{X}})$ . On the contrary, for wave vectors such that  $\mathbf{v}(\mathbf{k})$  is parallel to the local  $\mathbf{E}$  field, the distribution is far from the zero-temperature equilibrium of the thermostats. One can extract an effective temperature from the solution expressed in Eq. (16),  $T_{\text{eff}}(\mathbf{k}) \sim |\mathbf{E} \cdot \mathbf{v}(\mathbf{k})|/\Gamma$ , which depends on  $\mathbf{k}$ . In a

non-interacting metal, and in the weak-field limit, electrons traveling in the direction of the electric field are “hotter” than those traveling perpendicularly. Altogether, given that the electrons contributing most to transport are those at the Fermi surface, with velocity  $\mathbf{v}_F$ , we identify the effective temperature

$$T_{\text{eff}} \sim \frac{|\mathbf{E} \cdot \mathbf{v}_F|}{\Gamma}. \quad (18)$$

This expression can be approximately generalized to include corrections from the Coulomb interactions by renormalizing the bare electric field with Hartree-Fock corrections,  $\mathbf{E} \rightarrow \tilde{\mathbf{E}}_\sigma(\mathbf{X}) \equiv \mathbf{E} - \nabla_{\mathbf{X}} [U \langle n_{-\sigma}(\mathbf{X}) \rangle]$ , yielding in particular a dependence on the inhomogeneities of the non-equilibrium charge distribution.

- 
- [1] N. Tsuji, T. Oka, and H. Aoki, Phys. Rev. B **78**, 235124 (2008).
  - [2] C. Aron, G. Kotliar, and C. Weber, Phys. Rev. Lett. **108**, 086401(2012).
  - [3] J. E. Han and J. Li, Phys. Rev. B **88**, 075113 (2013).
  - [4] J. Li, C. Aron, G. Kotliar, and J. E. Han, Phys. Rev. Lett. **114**, 226403 (2015).
  - [5] B. K. Ridley, Proc. Phys. Soc. **82**, 954 (1963).
  - [6] H.-T. Kim, B.-J. Kim, S. Choi, B.-G. Chae, Y. W. Lee, T. Driscoll, M. M. Qazilbash, and D. N. Basov, J. Appl. Phys. **107**, 023702 (2010).
  - [7] A. Zimmers, L. Aigouy, M. Mortier, A. Sharoni, S. Wang, K. G. West, J. G. Ramirez, and I. K. Schuller, Phys. Rev. Lett. **110**, 056601 (2013).
  - [8] E. Janod, J. Tranchant, B. Corraze, M. Querré, P. Stoliar, M. Rozenberg, T. Cren, D. Roditchev, V. Ta Phuoc, M.-P. Besland, and L. Cario, Adv. Funct. Mater. **25** 6287 (2015).
  - [9] C. Zener, Proc. R. Soc. Lond. A **137**, 696 (1932).